Development and Preliminary In Vivo Study of 3D-Printed Bioactive Glass Scaffolds with Trabecular Architecture

ADVANCED ENGINEERING MATERIALS
www.aem-journal.com

Development and Preliminary In Vivo Study of 3D-Printed Bioactive Glass Scaffolds with Trabecular Architecture

*Dilshat Tulyaganov, Roberta Gabrieli, Avzal Akbarov, Nigora Nigmatova, Bekhzod Khabilov, Alessandro Schiavi, Martin Schwentenwein, Enrica Verné, and Francesco Baino**

The bioactive silicate glass "1d" (BG-1d), belonging to the multicomponent $CaO–MgO–Na_2O–P_2O_5–SiO_2–CaF_2$ system, is proved to be highly effective in promoting alveolar bone regeneration in humans when implanted in the form of particles. This study moves one step forward in developing BG-1d scaffolds with trabecular architecture by digital light processing-based vat photopolymerization to be then implanted in rabbit femora, which has never been reported so far. The scaffolds exhibit a clear osteogenic effect in vivo and undergo gradual resorption followed by ossification. Substantial resorption of scaffolds in favor of new bone formation is achieved within 3 months. These in vivo results support the suitability of BG-1d scaffolds for application in bone tissue engineering and, given the reproducibility and reliability of the 3D-printed devices, show promise for potential translation to the clinic.

1. Introduction

Bioactive glasses are an appealing class of biomaterials for bone tissue engineering due to their ability both to bond to living bone via an interfacial layer of nanocrystalline hydroxyapatite, which forms relatively fast (from hours to days) upon contact with biological fluids,[1] and to stimulate the regeneration of healthy tissue via the in vivo release of osteostimulatory ions such as Ca^{2+}, Mg^{2+}, and silicates.[2] "Exotic" ions can also be incorporated in bioactive glasses to elicit special extra-functionalities such as promotion of angiogenesis, antibacterial and anti-inflammatory effects, and anticancer therapy.[3]

Bioactive glasses are often processed to obtain 3D porous structures (implantable scaffolds) that support and guide the growth of healthy tissues while dissolving over time.[4] Melt-derived glass particles or colloidal suspensions in the sol-gel synthesis are typically processed by a molding/shaping method to introduce porosity, and then the resulting porous body is thermally treated to remove the organics and consolidate the structure. Conventional fabrication techniques include foaming,[5] removal of sacrificial particles,[6] and sponge replication.[7]

Over the last few years, additive manufacturing of bioactive glasses has significantly improved the quality and geometrical complexity of these porous bodies, allowing an accurate control over pore size/shape, thickness of solid walls, and thermal shrinkage to be achieved.[8] 3D-printed bioactive glass scaffolds have been mostly fabricated by the extrusion of glass/binder composite filaments that were deposited according to a grid-like architecture.[9] Depending on whether a thermal treatment is performed or not to burn off organics and sinter the glass particles, fully inorganic scaffolds[10] or porous polymer/glass composites[11] can be obtained. Silicate compositions are the most commonly used, but borate glass structures having faster reactivity with biofluids were also printed.[12] Bioprinting of cell-laden bioactive glass/natural polymer composites was also reported by using a robocasting-derived method.[13]

However, all these porous structures typically exhibit an arrangement of solid rods and parallel channels that does not properly replicate the trabecular structure of spongy bone, which is more similar to that of a foam with open spheroidal cells.[14] In this regard, additive manufacturing technologies based on vat photopolymerization are more suitable to obtain scaffolds with a 3D network of highly interconnected macropores.[15] Vat photopolymerization has been successfully applied to fabricate high-quality bone substitutes made of hydroxyapatite,[16] β-tricalcium phosphate,[17] and biphasic calcium phosphates.[18] Processing of

D. Tulyaganov
Department of Natural-Mathematical Sciences
Turin Polytechnic University in Tashkent
100095 Tashkent, Uzbekistan

R. Gabrieli, E. Verné, F. Baino
Institute of Materials Physics and Engineering
Department of Applied Science and Technology
Politecnico di Torino, 10129 Turin, Italy
E-mail: francesco.baino@polito.it

A. Akbarov, N. Nigmatova, B. Khabilov
Department of Prosthodontics
Tashkent State Medical University
100109 Tashkent, Uzbekistan

A. Schiavi
National Institute of Metrological Research (INRiM)
10135 Turin, Italy

M. Schwentenwein
Lithoz GmbH
1060 Vienna, Austria

The ORCID identification number(s) for the author(s) of this article can be found under https://doi.org/10.1002/adem.202501569.

DOI: 10.1002/adem.202501569

bioactive glasses by this method is highly appealing but still in its beginning; in a couple of previous research papers, we first used the tomographic reconstruction of a polyurethane sponge as the input file to the vat photopolymerization printing system to fabricate bioactive glass foams with pore volume ranging from 35 to 94 vol%.[19,20]

In the present work, we extended these promising results to print 3D porous implants based on the silicate composition "1d" (BG-1d), a multicomponent glass belonging to the CaO–MgO–Na_2O–P_2O_5–SiO_2–CaF_2 system; a comprehensive review on the design and applications of this specific biomaterial was recently provided elsewhere.[21] BG-1d is highly biocompatible in vitro, stimulating the viability and proliferation of mesenchymal stem cells as well as the osteogenic differentiation of cells in a comparable way to 45S5 Bioglass (benchmark).[22] In vivo tests both in animals (rabbits) and human patients (45 volunteers) proved the bone-regenerative capability of BG-1d particles.[23] The feasibility of macroporous BG-1d-derived scaffolds by using the conventional foam replica method[24] and vat photopolymerization[25] was recently reported, but these porous implants have never been tested in vivo until now: the goal of the current study is to bridge this gap and acquire further knowledge about the biological response elicited by these devices. Furthermore, to the best of the authors' knowledge, this is also the first study in which bioactive glass scaffolds produced by vat photopolymerization have been tested in vivo.

2. Experimental Section

2.1. Fabrication of BG-1d Glass Scaffolds

BG-1d material (composition: 46.1SiO_2-28.7CaO-8.8MgO-6.2P_2O_5-5.7CaF_2-4.5Na_2O wt%[26]), produced by the melt-quenching method, was selected for scaffold fabrication. The complete production process of the BG-1d powder is described in a previous work.[20]

After being sifted below 25 μm, glass powder was dispersed in a methacrylate matrix to formulate a photocurable slurry suitable for the additive manufacturing of the scaffolds. Specifically, porous structures were fabricated using digital light processing-based vat photopolymerization 3D-printing process (CeraFab 7500, Lithoz GmbH, Vienna, Austria), as previously reported;[20] each printing job included the production of 21 scaffolds which were thermally treated (debinding followed by sintering at 700 °C for 1 h) in an electrically-heated oven. Two printing jobs were run for this study (42 scaffolds produced in total) in order to have enough samples for performing all the characterizations described in the following sections, along some spare parts.

Porous cylindrical scaffolds (Ø 4.5 mm × h 4.5 mm) were designed from a micro-computed tomography (micro-CT)-based CAD model of a 45-ppi commercial polyurethane sponge; the geometry of this virtual template was uniformly scaled along the *X*, *Y*, and *Z* axes to match implantation requirements in rabbit bone, as defined by the drill diameter. As compared to the process reported in ref. [20] where scaffolds with very thin trabeculae were manufactured, a 25 μm contour offset was introduced to the foam structure during the design process in order to thicken the struts and make the mechanical strength suitable for in vivo implantation.

2.2. Morphological and Structural Characterization

The total porosity (volume percentage) of BG-1d scaffolds was calculated using the relation $(1 - \rho_{scaffold}/\rho_{material}) \times 100$, where $\rho_{scaffold}$ is the bulk density of the sample (determined as mass-to-volume ratio) and $\rho_{material}$ is the density of the nonporous material. The volume of each sintered scaffold was calculated from the geometrical measurements of diameter and height through a caliper. In order to assess $\rho_{material}$, dense reference samples were 3D-printed using BG-1d material and sintered at 700 °C for 1 h (under the same processing schedule used for making the scaffolds). Their density was measured using the Archimedes' method, and the obtained value for the solid BG-1d was $2.845 \pm 0.033\ g\ cm^{-3}$. Results were expressed as average ± standard deviation on 25 scaffolds.

Morphological investigations to analyze the pore-strut architecture of BG-1d sintered scaffolds were carried out by field-emission scanning electron microscopy (FESEM, Supra equipment, Zeiss, Germany) at an accelerating voltage of 5 kV. Scaffolds were sputtered with platinum prior to the analysis.

Quantification of structural parameters was obtained by micro-CT imaging, which was carried out on one representative scaffold using a custom-made setup available in the Interdepartmental Centre "J-Tech" at Politecnico di Torino. CT scanning parameters included a source voltage of 60 kV and a current of 200 μA, with a source-to-object distance (SOD) of 45 mm and a source-to-detector distance (SDD) of 900 mm; 800 projections were acquired at 0.45° increments with an exposure time of 1 s. Postprocessing including the image reconstruction and quantitative analysis was performed using VGStudio MAX 3.3 software (Volume Graphics, Heidelberg, Germany). An internal subvolume of the scaffold was selected to reduce surface artifacts. Microstructural analysis was then performed using the foam/powder analysis module, which enabled the segmentation and evaluation of pore structures, including quantification of pore diameter and wall thickness.

2.3. Mechanical Characterization

Mechanical performance of BG-1d scaffolds was evaluated through uniaxial compression tests, where the load was applied perpendicular to the cylinder base. The mechanical tests were performed on 9 scaffolds by using a custom-made stress-strain equipment built and available in the INRiM Institute in Turin (testing machine details are described in[27]). The measured values were obtained every 0.5 s, using a 50 N load cell and applying the load at a velocity of $\approx 0.005\ mm\ s^{-1}$. The peak compressive strength (σ) was calculated as the ratio between the maximum applied load during the test and the initial resistant cross-sectional area. In addition to the compressive strength, the Young's modulus was determined from the initial elastic deformation region of the stress–strain curve. Fracture energy per unit volume, namely the energy needed to deform the scaffold from the unloaded condition to the strain corresponding to the major

peak,[28] was calculated from the area under the stress–strain curve. Results were expressed as average ± standard deviation.

2.4. In Vivo Animal Tests

The animal care and surgeries were carried out following the ethical guidelines and rules of local Governmental bodies. The implantation was performed at the Tashkent Pharmaceutical Institute, Uzbekistan, while the histological analysis of the explanted bones with the scaffolds was completed at the Faculty of Prosthetic Dentistry, Tashkent State Dental Institute, Uzbekistan.

The permissions for performing in vivo biocompatibility tests were obtained by the State Unitary Enterprise "Center for Good Practices" of the Agency for the Development of the Pharmaceutical Industry at the Ministry of Health, Republic of Uzbekistan; certificate under reference GLP-02:2024 issued to the Tashkent Pharmaceutical Institute is valid from 09.08.2024 to 08.09.2027.

Healthy and completely matured (1-year-old) male rabbits from the breed "shinshilla," weighing 2.8–3.0 kg, were used throughout the experimental period. Animals were properly kept in individual cages before applying systemic anesthesia and then identified according to the period and group. Eighteen animals were segmented into 2 groups, namely experimental and control (9 animals in each one), while the procedure was split into 3 stages of observation of 1, 2, and 3 months according to **Table 1**.

Scaffolds designed according to the defect's geometry were sterilized in dry heat at 180 °C for 2 h and implanted in the femoral diaphysis region of each animal to fill a previously drilled hole of 4.0 mm diameter. Incision without any implantation with drilling a hole of 4.0 mm diameter was performed as a control.

An additional observation stage with 2 experimental animals was performed after 14 days of implantation to investigate the dynamics of bone resorption over time. At each timepoint, the rabbits were sacrificed by immediate decapitation. The surgeries and animal care were undertaken in accordance with ethical guidelines and rules of local governmental bodies. All femurs were subsequently fixed in 10% phosphate-buffered formalin for 72 h for histological or histomorphometrical analysis. These femurs were decalcified in 10% formic acid formalin solution for 14 days. The bones were sectioned parallel to the long axis of the femur through the anteromedial aspect of the defect. The tissue blocks were sectioned and stained with hematoxylin and eosin (H&E) and histopathologically observed by optical microscopy.

The following histological scoring scale was applied for statistical analysis, which considered the presence and intensity of bone formation:[29,30] 1, no osteogenesis; 2, weak osteogenesis; 3, medium-low osteogenesis; 4, medium-high osteogenesis; 5, good-low osteogenesis; 6, good-high osteogenesis; 7, perfect osteogenesis. Specifically, each slide of histopathological sections was divided into four segments to be observed in detail while the average of the scores of the four quadrants represents the overall score given to the slide.[29]

Since there were two groups—one was the experimental and the other was the control, statistical analysis was performed by using Wilcoxon–Mann–Whitney test.[29] The tests were performed with a level of significance of 5%. The test involves the calculation of a statistic, usually called U, whose distribution under the null hypothesis is known.[31]

3. Results and Discussion

3.1. Morphology and Porous Architecture

The planned process for scaffold fabrication allowed obtaining samples with suitable size and geometry for in vivo implantation in rabbits, according to the surgeons' recommendations. Specifically, the diameter and height of sintered BG-1d porous cylinders were 4.03 ± 0.04 mm and 4.14 ± 0.01 mm, respectively, with percentage ratios of standard deviation to average of 0.9% and 0.2% for these two geometrical dimensions, revealing an excellent reproducibility of the printing process for these challenging, small-sized samples.

The total porosity of BG-1d scaffolds was 77.2 ± 0.6 vol%, which falls in the typical range recommended for tissue engineering scaffolds addressed to bone regeneration (above 50 vol%).[32]

Morphological investigations reported in **Figure 1**A reveal that the 3D porous architecture of BG-1d scaffolds is actually a faithful replica of the cellular structure of the virtual template (CT reconstruction of a polyurethane sponge) and, in turn, mimics the structure of trabecular bone. As shown in Figure 1B, densification of struts is satisfactory although sporadic micrometric pores (pits) can be observed on the surface of scaffold struts, probably resulting from residual interparticle voids; however, their presence is expected to be beneficial from a biological perspective because it is well known that osteoblasts preferably attach to micro-rough implants.[33]

Figure 2 shows representative cross-sectional views obtained from micro-CT scan. The internal pores are segmented and color-coded based on their equivalent diameter, allowing quantitative assessment of pore morphology and size.

Pore size distribution in BG-1d scaffolds assessed by micro-CT analysis is reported in **Figure 3**A. The majority of pores were in the range of 200–800 μm, consistent with the recommendations that are generally followed for bone tissue engineering scaffolds (pore size below 900 μm for avoiding problems of structural integrity and suboptimal bone ingrowth).[34] A total of 320 pores

Table 1. Protocol followed for the implantation procedure.

Observation stage	Scaffold implantation (experimental)	Empty hall (control)
1 month	3 animals per group with numbering in the range № 1–3	3 animals per group with numbering in the range № 4–6
2 months	3 animals per group with numbering in the range № 7–9	3 animals per group with numbering in the range № 10–12
3 months	3 animals per group with numbering in the range № 13–15	3 animals per group with numbering in the range № 16–18

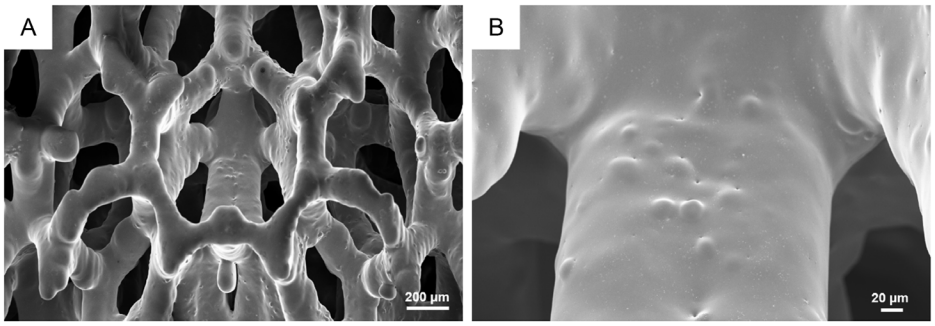

Figure 1. FESEM micrographs showing A) the 3D architecture (magnification 100×) and B) the strut surface of scaffolds (magnification 500×).

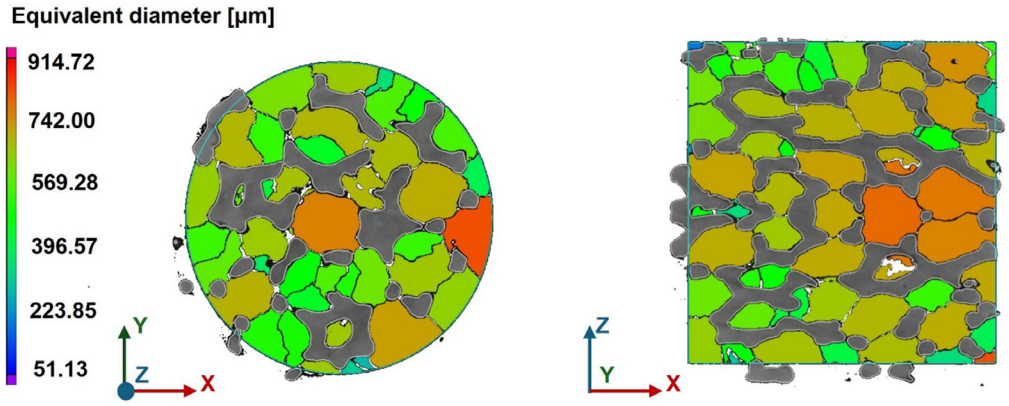

Figure 2. Micro-CT 3D reconstruction of a typical BG-1d scaffold showing internal pore segmentation within a porous structure through two orthogonal cross-sectional views.

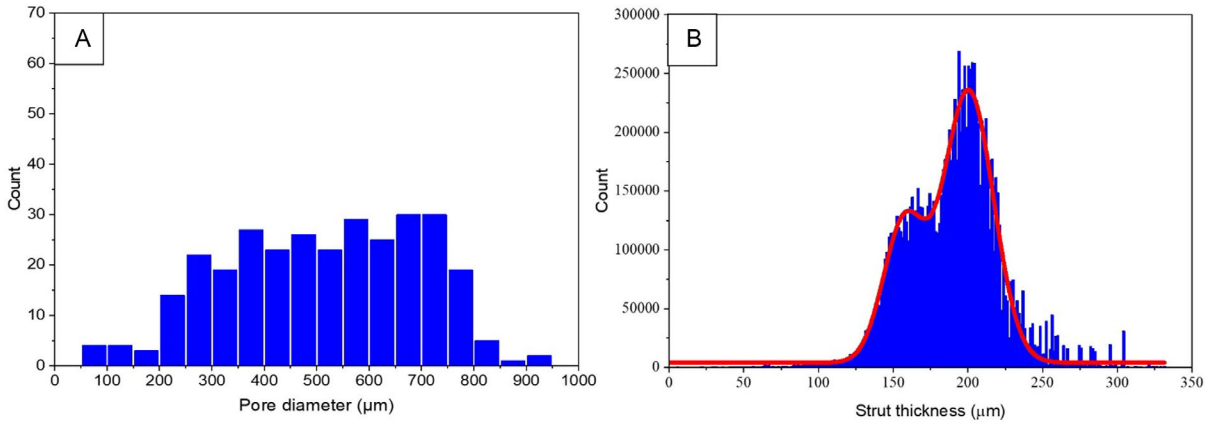

Figure 3. Results from micro-CT analysis on BG-1d scaffolds: distributions of A) pore size (diameter) and B) strut thickness (the red curve is the envelope of the distribution).

were measured, ranging from 70 to 910 µm, with an average value of 517 ± 183 µm.

CT scanning also allowed assessing the strut thickness distribution (Figure 3B), which exhibited two major peaks suggesting a bimodal distribution. A similar profile was already reported for scaffolds that were produced by the same 3D printing method using bioactive glass[19] or hydroxyapatite.[35] The first peak in Figure 3B (around 155 µm) can be attributed to the "true" diameter of a single strut (supposed to be rod-shaped), while the second peak (around 200 µm) is due to the "intersection" of two or multiple struts of the scaffold. The average value for strut thickness is 190 ± 32 µm.

3.2. Mechanical Properties

The compressive stress–strain curves for BG-1d scaffolds (an example is displayed in **Figure 4**A) exhibit a multipeaked profile,

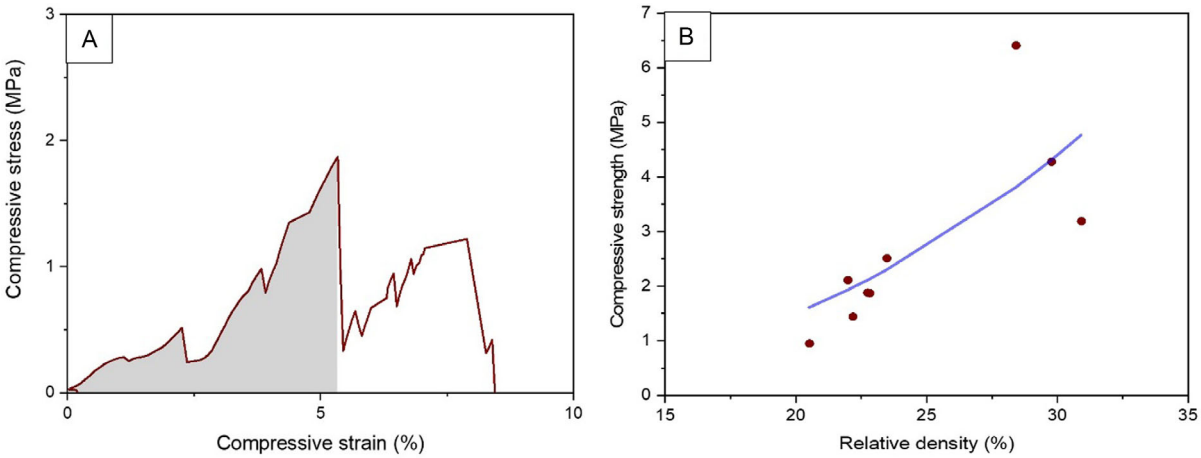

Figure 4. Results from mechanical tests: A) example of a typical stress–strain curve and B) modeling of experimental data (peak strength versus relative density).

which is typical of brittle porous materials like ceramics. This jagged profile illustrates the sequential fracture of scaffold struts during compression: an initial phase with a positive slope leading up to the major peak (1.83 MPa on average) is followed by a sudden drop in compressive stress indicating the fracture of the strut. When, after some fluctuations, the compressive stress returns to zero; this means that the sample is no longer in contact with the upper plate of the testing machine being fractured.

The elastic modulus estimated from the region of the graph before the major fracture peak was 70.3 ± 21.9 MPa, falling close to the lower threshold of the range which is typically considered for human spongy bone (50–500 MPa[36]).

The fracture energy of BG-1d scaffolds (calculated from the gray area in Figure 4A) was 43 ± 12 kJ m^{-3}; this value is lower than those assessed for other bioactive glass foams (540 kJ m^{-3}) that, however, were significantly less porous (56 vol%) and mechanically stronger.[37]

Figure 4B shows that the peak compressive strength is dependent on the relative density ($RD = \rho_{scaffold}/\rho_{material}$) of BG-1d scaffold: as the relative density increases, mechanical strength increases as well. The compressive strength is in the range of 1.7–4.8 MPa, which is consistent with the typical values for human spongy bone (0.1–16 MPa).[38] Figure 4B also includes data interpolation through the Gibson–Ashby power-law model (Equation (1)), which is commonly used to describe the mechanical behavior of brittle foams[39]

$$\sigma = \sigma_0 C_1 (RD)^n \quad (1)$$

where C_1 and n are the model constants and σ_0 is the compressive strength of nonporous BG-1d. The fitting of experimental data to determine the parameters $C_1 = 0.127$ and $n = 2.66$ (see the curve in Figure 4B) was carried out using a proper code developed in MATLAB based on the least squares method. The coefficient of determination $R^2 = 0.556$ suggests an acceptable accuracy and fair predictive capability of the power-law model for the compressive strength of 3D-printed BG-1d scaffolds.

3.3. In Vivo Studies (Animal Model)

The rabbits exhibited ordinary behavior over the whole implantation period, with no reports of adverse effects such as allergies or other immunologic reactions, abscess formation, or rejection of the scaffold. The following characteristic features were analyzed during the observation of tissue blocks under optical microscopy: 1) the presence of inflammatory infiltrate, 2) the woven bone formation in the margins of the wound, 3) the woven bone formation in the center of the wound, and 4) the transformation of woven bone to laminar bone. Histological examination of the rabbit femur with an implanted bioactive glass scaffold after 1 month postimplantation revealed preservation of the bioactive glass in the form of light-eosinophilic fine-granular content. Scaffold residues were in various-sized cellular structures formed by maturing trabeculae of lamellar bone tissue (**Figure 5**). However, under higher magnification in areas bordering the implant, we observed larger, basophilic fragments of an amorphous substance surrounded by woven bone with weak inflammatory infiltration. This is consistent with previous observations by the authors[40] as well as other research groups[41–43] who investigated different bioactive glass compositions in vivo.

Histological examination of a rabbit femur with an implanted bioactive glass scaffold after 2 months postimplantation revealed considerable resorption of the scaffold with the implant pores being replaced by woven bone tissue (**Figure 6**). Under higher magnification (Figure 6B,C), scaffold material remnants are observed in the form of fine granularity in isolated cells (e.g., indicated as black asterisk). Bone trabeculae are thicker and characterized by an ordered lamellar structure formed from concentric-parallel lamellae evidencing that woven bone was gradually substituted by lamellar bone. Isolated bright eosinophilic foci of calcifications are noted.

Histological examination of a rabbit femur with an implanted bioactive glass scaffold after 3 months postimplantation revealed substantial resorption of the implant with the replacement of the cavities between the thickened mature beams with bone marrow tissue (**Figure 7**). Apparently, dissolution of BG-1d scaffolds is

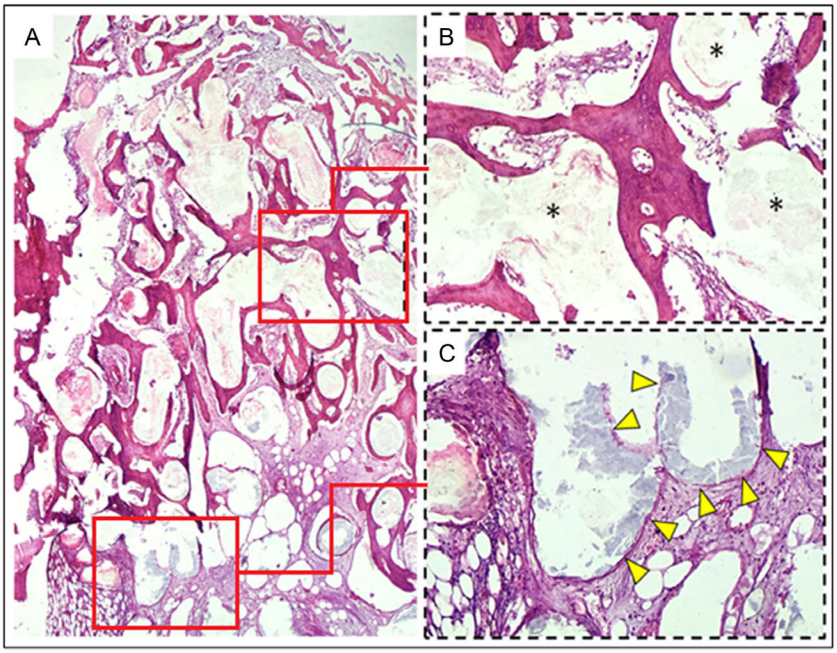

Figure 5. Histological examination (H&E staining) of a rabbit femur preparation with an implanted bioactive glass scaffold after 1 month postimplantation: A) The histopathological changes are characterized by the presence of areas with more matured bone trabeculae (inset "B"), as well as peripheral areas of woven bone tissue (inset "C"), formed around residual masses of bioactive glass (magnification 40×). B) Scaffold residues in the central areas, surrounded by bone trabeculae, are presented in the form of light-eosinophilic fine-granular content (black asterisk) (magnification 100×). C) Scaffold residues in the peripheral areas are in the form of larger, basophilic fragments of amorphous substance (pointed with the yellow arrowheads), surrounded by woven bone with weak mononuclear infiltration (magnification 100×).

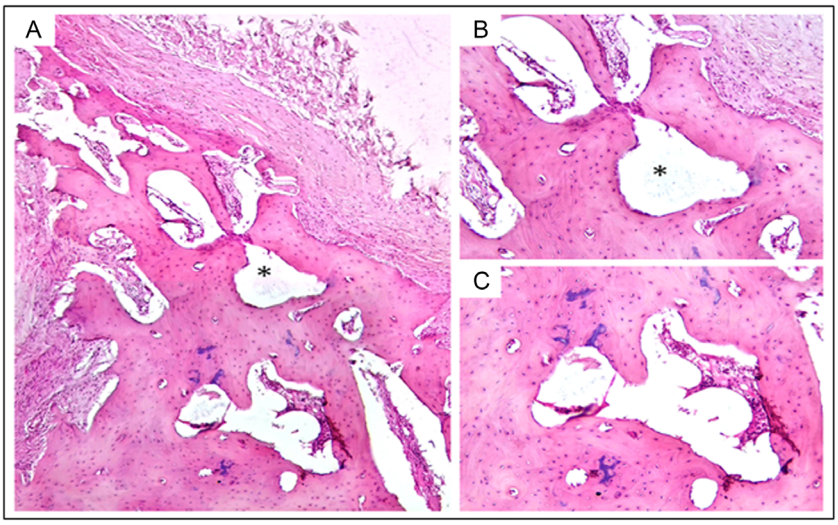

Figure 6. Histological examination (H&E staining) of a rabbit femur preparation with an implanted bioactive glass scaffold after 2 months postimplantation. Thickened bone trabeculae are visible, between which there are spaces filled with woven bone tissue containing mononuclear cells. In single cells, fine-grained particles of scaffold material remnants are observed (black asterisk). Magnification: A) 100× and B,C) 200×.

more intensive than that observed in the case of BG-1d particles implanted in rabbits of the same breed (glass residues were still observed at 3–4 months postimplantation[23]).

The dynamics of pathomorphosis of a rabbit femur preparation with an implanted bioactive glass scaffold on days 14, 30, 60, and 90 are shown in **Figure 8**. The areas where particles of scaffold material remnants were clearly revealed are indicated with black asterisks. The dynamics of pathomorphosis show that gradual resorption of scaffold material occurred from the first weeks of implantation (Figure 8A,B), reaching its substantial phase after 3 months postimplantation (Figure 8D). Nevertheless, further investigations for longer periods of

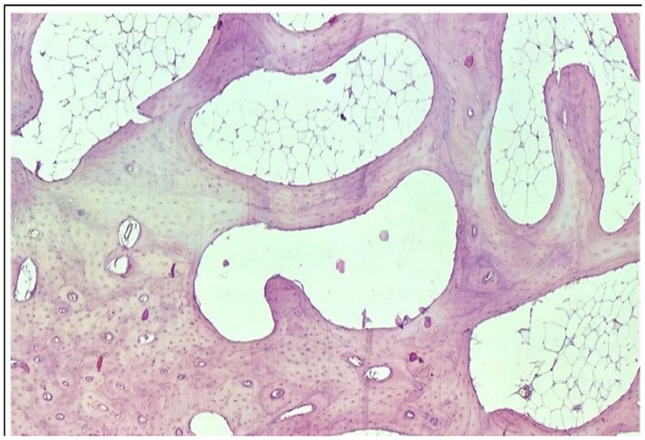

Figure 7. Histological examination (H&E staining) of a rabbit femur preparation with an implanted bioactive glass scaffold, after 3 months postimplantation. Substantial resorption of the bioactive glass scaffold was observed (magnification 100×).

implantation time are needed to better evaluate scaffold resorption.

Delayed regeneration compared to the experimental group was revealed in the control group (**Figure 9**), revealing the presence of immature connective tissue in the defect area.

One of the most important findings from the histological examinations is that a BG-1d scaffold-implanted defect showed a more homogenous tissue formation throughout the entire defect when compared to the control with signs of a high level of osteointegration and a medullary cavity occupied with bone marrow after 3-month postimplantation.

Wilcoxon–Mann–Whitney test, which was used to perform statistical analysis (data for calculation are shown in **Table 2**), showed that U calculated $\leq$ U critical always, that is, the calculated U values were either equal to or lower than the critical tabulated U values. Therefore, it was suggested that there is a statistically significant difference between the intensity of bone formation score in the control and the experimental groups with BG-1d scaffolds at all 3 tested periods of implantation (Table 2). Moreover, the "osteogenic effect" associated with the scaffold implantation is statistically significant, real, and not due to chance.

In general, the process of bone fracture healing includes first the development of an acute inflammatory response, followed by the recruitment of mesenchymal stem cells (MSCs), the generation of cartilaginous bony callus, the mineralization of the extracellular matrix (ECM), revascularization/angiogenetic processes, resorption of cartilaginous callus, and finally bone remodeling.[44,45] Specifically, when bone tissue is injured by drilling a defect through one cortex of the diaphysis of a young rabbit femur, the blood vessels inside the bone defect are disrupted and the blood enters the bone defect area, thus forming a hematoma. Inside the defect, macrophages and their recruited immune cells mediate inflammatory reactions, playing the most crucial role in this stage.[42] When the inflammatory phase is

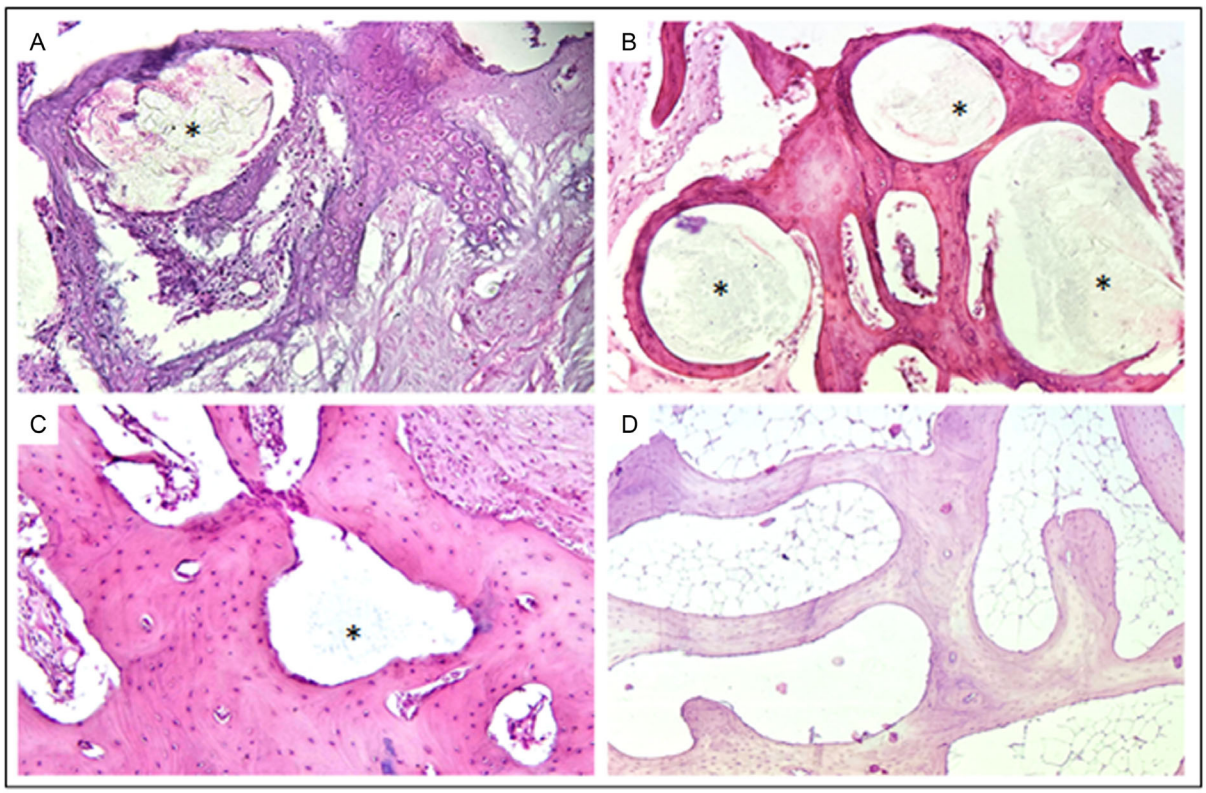

Figure 8. Dynamics of pathomorphosis of a rabbit femur preparation with an implanted bioactive glass scaffold on days 14, 30, 60, and 90. Hematoxylin and eosin staining, magnification 100×. The particles of scaffold material remnants are indicated with black asterisks.

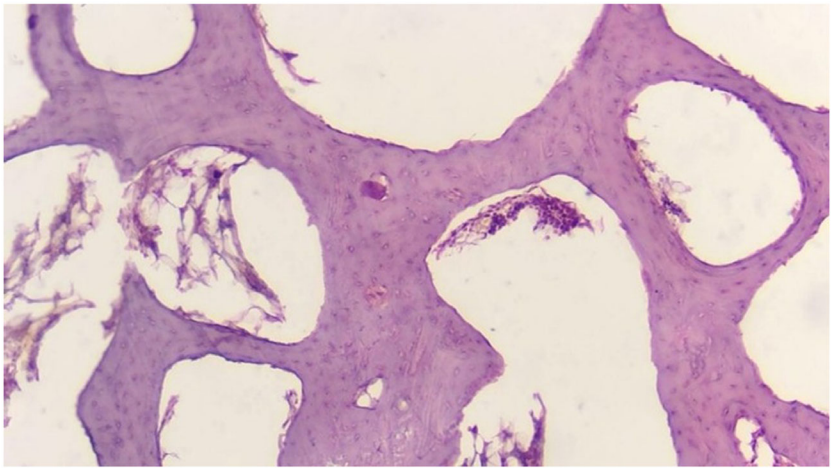

Figure 9. Histological examination (H&E staining) of a rabbit femur preparation in the control group after 3 months (magnification 100×).

Table 2. Bone formation scores for experimental and control groups according to the design of the implantation procedure (Table 1) and histological scoring scale (Section 2.4).

Observation stage (timepoint)	Scaffold implantation (experimental)	Empty hall (control)
1 month	№ 1/score 3	№ 4/score 2
	№ 2/score 3	№ 5/score 2
	№ 3/score 3	№ 6/score 1
2 months	№ 7/score 4	№ 10/score 3
	№ 8/score 4	№ 11/score 2
	№ 9/score 4	№ 12/score 3
3 months	№ 13/score 5	№ 16/score 3
	№ 14/score 5	№ 17/score 4
	№ 15/score 6	№ 18/score 4

completed, bone tissue gradually enhances the anabolic and repair processes while cellular components involved in bone regeneration in the granulation tissue include fibroblasts, osteoprogenitor cells, and MSCs.[46] Fibroblasts proliferate and secrete a fibrous matrix, gradually replacing the granulation tissue with a fibrous tissue of enhanced mechanical strength. MSCs recruited from the bone marrow, periosteum, adjacent soft tissues, and peripheral circulation aggregate and proliferate.[47] They further differentiate into chondrocytes and secrete a semi-rigid avascular cartilage matrix, gradually transforming the fiber-rich granulation tissue into a fibrocartilage- and hyaline cartilage-rich soft callus. Undifferentiated MSCs lie parallel to the fibrinous arcade, in conjunction with vascularization. Furthermore, transformation from undifferentiated MSCs to mesenchymal osteoblasts, with increasing woven tissue synthesis, and eventually to surface osteoblasts synthesizing lamellar bone on woven bone, was revealed. Finally, remodeling of the woven bone into lamellar bone may occur over the course of months to years and allows for restoration of the canal and its bony properties.[45] Bone remodeling is the last phase of bone healing and is also known as the secondary bone formation, which includes the reconstruction of the hard callus into the lamellar bone and the change of configuration of the cancellous bone trabeculae.[42]

Bone tissue engineering scaffolds can play a key role as 3D templates that allow cells to attach, proliferate, differentiate, and organize into normal, healthy bone as the scaffold degrades. The scaffold degradation rate must be tailored to match the rate of regeneration of new tissue.[48] The strong crystallization tendency of two well-known commercial bioactive glasses like 45S5 and S53P4 limits their hot-working into amorphous scaffolds. Thus, unreacted and partially crystallized 45S5 glass has been found several months after implantation in rabbit femurs.[49] Similar findings were reported for clinical studies of S53P4.[50,51] In fact, crystallization reduces the dissolution rate compared with the parent (amorphous) bioactive glass.[52,53]

The preliminary in vivo testing results reported in the present study support the capability of BG-1d scaffolds to act as an inherently osteoinductive biomaterial stimulating bone regeneration in noncritical-sized defects. Although a relatively fast rate of degradation was revealed within 3 months, further investigations are needed to evaluate the integration of bioactive glass scaffolds with host bone when implanted for longer periods of time.

Looking at the future, two advanced in vivo studies will deserve to be carried out in order to 1) compare the performances of BG-1d scaffolds with those of a reference biomaterial (having the same 3D porous trabecular architecture) to demonstrate the advantages of this new material over the state of the art and 2) compare the performances of at least two BG-1d scaffold batches with different architecture, for example, foam versus grid. In the study (1), an option might be the use of the well-known Hench's 45S5 glass as a control, although the fabrication of 45S5-derived foams is challenging as this glass has a high tendency to crystallize during sintering,[53] which leads to low densification of struts and poor mechanical properties. The study (2) will be key to elucidate what might be the optimal porous architecture for bone scaffolds: at present, this question is still under debate in the scientific community and none can definitely state that a porous arrangement of open pores is superior in stimulating bone regeneration over another configuration.[54]

Furthermore, micro-CT scanning or radiological imaging could be useful to show the regeneration of new bone in the defect sites without sacrificing the animals.

4. Conclusions

3D printing via digital light processing-based vat photopolymerization allowed the successful production of bioactive glass scaffolds with bone-like trabecular architecture. The samples, derived from the BG-1d composition, showed high reproducibility and mechanical properties comparable to those of human cancellous bone, making them promising for bone repair. Histological analysis following implantation in rabbits demonstrated that there was a statistically significant difference between the intensity of bone formation score in the control and the experimental groups at all 3 tested periods of implantation (1, 2, and 3 months). BG-1d scaffolds elicited an osteogenic effect and were prone to substantial resorb within 3 months postimplantation. New homogeneous dense tissue similar to laminar bone, which was formed after 3 months at the expense of bone graft, demonstrated high level of osteointegration of the implant and suggests the potential application of BG-1d scaffolds in osteostimulatory bone healing.

Acknowledgements

D.T. and R.G. contributed equally to this work. Mr. Federico Gaido is acknowledged for his assistance during the preparation of the samples.

Open access publishing facilitated by Politecnico di Torino, as part of the Wiley - CRUI-CARE agreement.

Conflict of Interest

The authors declare no conflict of interest.

Data Availability Statement

The data that support the findings of this study are available from the corresponding author upon reasonable request.

Ethics Approval Statement

The animal care and surgeries were carried out following the ethical guidelines and rules of local Governmental bodies. The permissions for performing in vivo biocompatibility tests were obtained by the State Unitary Enterprise "Center for Good Practices" of the Agency for the Development of the Pharmaceutical Industry at the Ministry of Health, Republic of Uzbekistan; certificate under reference GLP-02:2024 issued to the Tashkent Pharmaceutical Institute is valid from 09.08.2024 to 08.09.2027.

Keywords

bioactive glasses, in vivo, scaffolds, vat photopolymerization

Received: July 1, 2025
Published online:

[1] L. L. Hench, *J. Mater. Sci.: Mater. Med.* **2006**, *17*, 967.
[2] A. Hoppe, N. S. Güldal, A. R. Boccaccini, *Biomaterials* **2011**, *32*, 2757.
[3] U. Pantulap, M. Arango-Ospina, A. R. Boccaccini, *J Mater Sci Mater Med* **2022**, *33*, 3.
[4] Q. Fu, E. Saiz, M. N. Rahaman, A. P. Tomsia, *Mater. Sci. Eng.: C* **2011**, *31*, 1245.
[5] G. Poologasundarampillai, P. D. Lee, C. Lam, A.-M. Kourkouta, J. R. Jones, *Int. J. Appl. Glass Sci.* **2016**, *7*, 229.
[6] F. Baino, E. Vernè, C. Vitale-Brovarone, *Mater. Sci. Eng.: C* **2009**, *29*, 2055.
[7] E. Boccardi, A. Philippart, J. A. Juhasz-Bortuzzo, G. Novajra, C. Vitale-Brovarone, A. R. Boccaccini, *Adv. Appl. Ceram.* **2015**, *114*, S56.
[8] R. Gmeiner, U. Deisinger, J. Schönherr, B. Lechner, R. Detsch, A. R. Boccaccini, J. Stampfl, *J. Ceram. Sci. Technol.* **2015**, *6*, 75.
[9] A. Motealleh, S. Eqtesadi, A. Civantos, A. Pajares, P. Miranda, *J. Mater. Sci.* **2017**, *52*, 9179.
[10] Q. Fu, E. Saiz, A. P. Tomsia, *Acta Biomater.* **2011**, *7*, 3547.
[11] T. Distler, N. Fournier, A. Grünewald, C. Polley, H. Seitz, R. Detsch, A.R. Boccaccini, *Front. Bioeng. Biotechnol.* **2020**, *8*, 552.
[12] K. C. R. Kolan, Y. W. Huang, J. A. Semon, M. C. Leu, *Int. J. Bioprint.* **2020**, *6*, 1.
[13] K. C. R. Kolan, J. A. Semon, B. Bromet, D. E. Day, M. C. Leu, *Int. J. Bioprint.* **2019**, *5*, 3.
[14] N. Reznikov, R. Shahar, S. Weiner, *Acta Biomater.* **2014**, *10*, 3815.
[15] F. Baino, G. Magnaterra, E. Fiume, A. Schiavi, L. P. Tofan, M. Schwentenwein, E. Verné, *J. Am. Ceram. Soc.* **2021**, *105*, 1648.
[16] L. D'Andrea, R. Gabrieli, L. Milano, L. Magagnin, A. De Cet, D. Alidoost, M. Schwentenwein, E. Verne', F. Baino, P. Vena, *Acta Mater.* **2025**, *287*, 120776.
[17] D. Schönegg, H. Essig, A. Al-Haj Husain, F. E. Weber, S. Valdec, *Int. J. Implant Dent.* **2024**, *10*, 21.
[18] Y. Wang, Y. Liu, S. Chen, M-F. Francis Siu, C. Liu, J. Bai, M. Wang, *Bioact. Mater.* **2025**, *46*, 21.
[19] F. Baino, J. Dias, M. Alidoost, M. Schwentenwein, E. Verné, *Open Ceram.* **2023**, *15*, 100392.
[20] F. Baino, F. Gaido, R. Gabrieli, D. Alidoost, A. Schiavi, M. Mohammadi, M. Schwentenwein, D. Tulyaganov, E. Verné, *Open Ceram.* **2024**, *20*, 100690.
[21] D. U. Tulyaganov, S. Agathopoulos, K. Dimitriadis, H. R. Fernandes, R. Gabrieli, F. Baino, *The Story, Properties And Applications Of Bioactive Glass '1d': From Concept To Early Clinical Trials*, *Inorganics.* **2024**, *12*, 224. https://doi.org/10.3390/inorganics12080224.
[22] S. I. Schmitz, B. Widholz, C. Essers, M. Becker, D.U. Tulyaganov, A. Moghaddam, I. Gonzalo de Juan, F. Westhauser, *Bioact. Mater.* **2020**, *5*, 55.
[23] D. Tulyaganov, M. Makhkamov, A. Urazbaev, A. Goel, J. Ferreira, *Ceram. Int.* **2012**, *39*, 2519.
[24] F. Baino, D. U. Tulyaganov, Z. Kahharov, A. Rahdar, E. Verné, *Ceram.* **2022**, *5*, 120.
[25] A. Schiavi, F. Gaido, R. Gabrieli, D. Alidoost, M. Schwentenwein, M. Mohammadi, D. Tulyaganov, E. Verne, F. Baino, *Mater. Lett.* **2025**, *384*, 138064.
[26] I. Kansal, D. U. Tulyaganov, A. Goel, M. J. Pascual, J. M. F. Ferreira, *Acta Biomater.* **2010**, *6*, 4380.
[27] A. Schiavi, A. Prato, *Polym. Test* **2017**, *59*, 220.
[28] P. Kenesei, C. Kádár, Z. Rajkovits, J. Lendvai, *in Scr. Mater.* **2004**, *50*, 295.
[29] A. F. de França Camargo, A. M. Baptista, R. Natalino, O. P. de Camargo, *Acta Ortop. Bras.* **2015**, *23*, 202.
[30] D. Bellucci, V. Cannillo, A. Anesi, R. Salvatori, L. Chiarini, T. Manfredini, D. Zaffe, *Materials* **2018**, *11*, 2223.
[31] N. Nachar, The Mann-Whitney U: A Test for Assessing Whether Two Independent Samples Come from the Same Distribution,*Tutorials in Quantitative Methods for Psychology* **2008**, *4*, 13-20.
[32] V. Karageorgiou, D. Kaplan, *Biomaterials* **2005**, *26*, 5474.
[33] Z. Schwartz, B. D. Boyan, *J. Cell Biochem.* **1994**, *56*, 340.
[34] T. M. Koushik, C. M. Miller, E. Antunes, *Adv. Healthc. Mater.* **2023**, *12*, 2202766.

[35] A. Schiavi, E. Fiume, G. Orlygsson, M. Schwentenwein, E. Verné, F. Baino, *J. Eur. Ceram. Soc.* **2022**, *42*, 6206.
[36] I. D. Thompson, L. L. Hench, *Proc. Inst. Mech. Eng. H* **1998**, *212*, 127.
[37] F. Baino, C. Vitale-Brovarone, *Mater. Lett.* **2014**, *118*, 27.
[38] L. C. Gerhardt, A. R. Boccaccini, *Materials* **2010**, *3*, 3867.
[39] L. J. Gibson, *Mater. Sci. Eng.: A* **1989**, *110*, 1, doi: 10.1016/0921-5093(89)90154-8.
[40] D. U. Tulyaganov, E. Fiume, A. Akbarov, N. Ziyadullaeva, S. Murtazaev, A. Rahdar, J. Massera, E. Verné, F. Baino, *J. Funct. Biomater.* **2022**, *13*, 74.
[41] M. C. Crovace, M. T. Souza, C. R. Chinaglia, O. Peitl, E. D. Zanotto, *J. Non Cryst. Solids* **2016**, *432*, 90.
[42] G. Zhu, T. Zhang, M. Chen, K. Yao, X. Huang, B. Zhang, Y. Li, J. Liu, Y. Wang, Z. Zhao, *Bioact Mater.* **2021**, *6*, 4110.
[43] J. T. Heikkilä, H. J. Aho, A. Yli-urpo, R. P. Happonen, A. J. Aho, *Acta Orthop.* **1995**, *66*, 463.
[44] J. R. Perez, D. Kouroupis, D. J. Li, T. M. Best, L. Kaplan, D. Correa, *Tissue Engineering And Cell-Based Therapies For Fractures And Bone Defects*, Frontiers in Bioengineering and Biotechnology. **2018**, 6. https://doi.org/10.3389/fbioe.2018.00105.
[45] F. Shapiro, J. Y. Wu, *Eur. Cell Mater.* **2019**, *38*, 137.
[46] T. A. Einhorn, L. C. Gerstenfeld, *Fracture healing: Mechanisms and interventions*, *Nature Reviews Rheumatology*. **2015**, *11*, 45-54. https://doi.org/10.1038/nrrheum.2014.164.
[47] A. Schindeler, M. M. McDonald, P. Bokko, D. G. Little, *Bone Remodeling During Fracture Repair: The Cellular Picture*, *Seminars in Cell & Developmental Biology*. **2008**, *19*, 5. https://doi.org/10.1016/j.semcdb.2008.07.004.
[48] J. Will, L. C. Gerhardt, A. R. Boccaccini, *Bioactive Glass-Based Scaffolds For Bone Tissue Engineering, Advances in Biochemical Engineering Biotechnology*. **2012**, *126*. https://doi.org/10.1007/10_2011_106.
[49] D. L. Wheeler, E. J. Eschbach, R. G. Hoellrich, M. J. Montfort, D. L. Chamberland, *J. Orthop. Res.* **2000**, *18*, 140.
[50] L. Aalto-Setälä, M. Siekkinen, N. Lindfors, L. Hupa, *Biomed. Mater. Devices* **2023**, *1*, 871.
[51] N. C. Lindfors, I. Koski, J. T. Heikkilä, K. Mattila, A. J. Aho, *J. Biomed. Mater. Res. B Appl. Biomater.* **2010**, *94B*, 157.
[52] O. Peitl, E. Dutra Zanotto, L. L. Hench, *J. Non-Cryst. Solids* **2001**, *292*, 115.
[53] J. Massera, S. Fagerlund, L. Hupa, M. Hupa, *J. Am. Ceram. Soc.* **2012**, *95*, 607.
[54] F. Baino,R. Gabrieli, E. Verné, A. Schiavi, M. Schwentenwein, L. D'Andrea, P. Vena, *Ceram. Int.*, **2025**, *51*, 12355.